JOURNAL OF COMPUTATIONAL PHYSICS **144,** 484–516 (1998)
ARTICLE NO. CP986000

An Efficient Multigrid Algorithm for Compressible Reactive Flows

Scott G. Sheffer, Luigi Martinelli, and Antony Jameson

Department of Mechanical and Aerospace Engineering, Princeton University, Princeton, New Jersey 08544
E-mail: sheff@mig.Princeton.edu, gigi@phantom2.Princeton.edu, and jameson@hornet.Princeton.edu

Received June 27, 1997; revised March 25, 1998

This paper presents a parallel multigrid method for computing inviscid and viscous high speed steady-state reactive flows. The governing equations for reactive flow are solved using an explicit multigrid algorithm while treating the chemical source terms in a point implicit manner. The CUSP (Convective Upwind and Split Pressure) scheme is used to provide necessary artificial dissipation without contaminating the solution. This explicit method yields excellent parallel speedups, thus enabling the calculation of reactive flows with detailed chemical kinetics including large numbers of species and reactions. Results indicate good multigrid speedups and adequate resolution of the reaction zone in both inviscid axisymmetric and viscous two-dimensional hydrogen/oxygen and hydrogen/air test cases.

1. INTRODUCTION

The simulation of high speed chemically reacting flows is a very challenging area for computational methods. The presence of shock waves necessitates good shock capturing properties, while excessive numerical dissipation must be avoided in the treatment of chemical reactions so that the solution remains uncontaminated. Viscous effects, heat conduction, and species diffusion complicate reactive flow calculations, both from the increased computational work required and because of possible interactions between the chemistry and these effects. Diffusion of radical species in a boundary layer may significantly alter the resulting flowfield. Exponential increases and decreases of radical species in small spatial zones lead to large gradients that must simultaneously be captured without oscillation and without unnecessary dissipation. In addition, there is usually a great disparity between the characteristic time scales of the chemical source terms and the characteristic times of the convective and diffusive portions of the governing equations. This "stiffness" makes the integration of the governing equations very difficult and time consuming.

Stiffness may be viewed in terms of characteristic times. If two processes exist in the same system, but the first has a very short characteristic time while the second has a much

0021-9991/98 $25.00

longer characteristic time, then it is clear that after a short period of time, the first process will have been completed. Thus, further change in the solution is only determined by the second process and it would only be necessary to use the second mode to further advance the solution. Therefore, in terms of accuracy, only the second mode is important after the first mode has reached an "equilibrium" state. However, for the numerical solution of the system, the stability requirements of the scheme necessitate retaining both modes. The time step limitation of the scheme is based on the fastest mode, which means that the system is being simulated at an exceptionally slow rate. This conflict between acceptable accuracy and necessary stability is the heart of stiff problems [12]. Stiffness is not only a problem in chemically reacting flows; the large disparity of characteristic times in nearly incompressible flows in one reason for the slow convergence rates and loss of accuracy of hyperbolic solvers at low Mach numbers [1]. Artificial compressibility is a way of removing the inherent stiffness of incompressible flows by preconditioning the equations to attain higher convergence rates with a hyperbolic solver.

Because most of the detailed chemical mechanisms contain chemical reactions which evolve over characteristic times much smaller than those of the convective flow field, many explicit schemes are handicapped in computing such flows. In fact, while the thickness of the reaction zone is controlled by the slowest reactions, stiffness may be present within the mechanism as some modes may decay very rapidly while others have longer lifetimes. The time step for an explicit scheme is proportional to the shortest characteristic time, so that stability restrictions require very short time steps in reactive flow simulations. This short time step leads to very long simulation times for steady state computations.

Several ways to overcome this limitation of explicit schemes for chemically reacting flows have been explored. Gear [12] recognized that treating a stiff system implicitly would remove time step limitations for stability purposes and allow the time step to be chosen on the basis of accuracy requirements. Thus, one way to remove stability limitations for the simulation of chemically reacting flow is to use a fully implicit scheme. Wilson and MacCormack [38] used such a scheme with Gauss–Seidel line relaxation to compute steady hydrogen/air combustion over high speed blunt projectiles. Shuen and Yoon [32] used a Lower-Upper Symmetric Successive Overrelaxation (LU-SSOR) implicit factorization scheme to compute premixed and non-premixed chemically reacting flow including viscous effects. Yungster [43] used an LU-SSOR scheme to compute shock-wave/boundary layer interactions in premixed combustible gas flows. Yungster and Rabinowitz [46] used the same LU-SSOR scheme to simulate high speed methane/air combustion over blunt bodies and ram accelerator configurations. Ju [18] implemented a Lower-Upper Symmetric Gauss-Seidel (LU-SGS) scheme to calculate several reactive viscous flows.

Due to the large allowable time step of an implicit scheme, all of these methods may converge to a steady state solution in fewer time steps than an explicit method. However, these implicit methods entail inverting large numbers of matrices. Most link the solution domain together in a way that may hamper efficient parallelization. For unsteady simulations, the restriction on the time step for time accuracy may be the dominant factor, removing the advantage gained by the unconditional stability of the implicit scheme. In addition, during the initial stages of a steady state simulation, growing modes (such as production of radicals) may require the time step to be set by accuracy requirements instead of stability requirements which would again lower the advantage of having a large allowable time step from stability considerations.

Another way of reducing the effect of the chemical term stiffness is to treat the source term in a point implicit manner. In this formulation, due to Bussing and Murman [2, 3], the source term at the next time level is linearized about the current time level, leading to a fully explicit equation at the cost of a matrix inversion. This action has the effect of preconditioning the species continuity equations, rescaling the chemical characteristic time so that it is of the same order as the convective characteristic time. Thus, the entire system may be advanced using a time step based on the spectral radii of the convective and diffusive portions of the governing equations. Palmer and Venkatapathy [28] performed a study of high speed dissociating air using both the fully implicit and point implicit approach. They found that, at higher Mach numbers, the fully implicit scheme would not converge unless its time step was drastically reduced while the point implicit scheme was very robust and converged at all Mach numbers at its time step limit.

Numerous investigators have used the point implicit approach for both steady state [8, 44, 45] and unsteady simulations [26, 39]. Wilson and Sussman [39] combined the point implicit treatment with a formulation of the species conservation equations in logarithmic form. Thus, exponential increases and decreases of radical species in the induction zone were captured quite well. However, the resulting numerical method is not fully conservative and necessitates the introduction of elemental conservation equations. Sussman [33] modified the evaluation of the chemical source term so that the error of a finite difference scheme would be approximately cancelled, leading to higher accuracy and lower grid requirements. This modification was combined with the point implicit treatment of the source term to yield a very accurate scheme for the simulation of unsteady reactive blunt body flows.

Bussing and Murman also approximated the source term Jacobian matrix by using only its diagonal elements [3]. A considerable savings in computing time was achieved, but the approximation introduces some inaccuracies in the time scaling of the species equations. If these inaccuracies are severe enough, the scheme may become unstable. Eklund *et al.* [7] investigated several variants of the point implicit procedure. Eberhardt and Imlay [6] suggested scaling the linearized time step by a characteristic time for each species equation and Ju [18] offered a means for approximating the characteristic time for each species.

Another option to ameliorate the effects of stiffness is to split the reactive portion and the non-reactive portion of the governing equations and use different solvers on each portion [27]. Thus, a stiff equation solver or asymptotic method could be used for the ordinary differential equations that include the chemical source terms and a highly optimized flow solver could be used for the convective and dissipative parts of the governing equation. The flow field evolution takes place while the chemistry is frozen and then the chemistry is advanced while the flow field is held constant.

The inherent inaccuracy of chemical rate data presents another challenge to modeling reactive flows. The turn around time of reactive flow simulations must be made short enough so that varying rate coefficients may be examined in order to determine which set is the most appropriate for modeling a particular phenomena.

The use of multigrid acceleration for reactive flow calculations has not been adequately examined. Bussing and Murman [3] explored the use of multigrid, but only for their one-dimensional calculations. Multigrid techniques may have been thought to be too dissipative and cause radical species to be moved to physically incorrect regions. However, proper multigrid techniques [29, 30], in which the coarse grids are forced by the fine grid solution, can in fact be used to compute chemically reacting flows. With the addition of viscous

effects and species diffusion to reactive flows and the use of detailed chemical models, a way to accelerate convergence is sorely needed. While parallelization will decrease the computational time associated with a numerical simulation, multigrid techniques represent an untapped potential for convergence acceleration of reactive flow calculations.

The accurate capture of shock waves and large gradients in species concentrations necessitates non-oscillatory numerical dissipation schemes that do not overly dissipate the solution. Unphysical diffusion of radical species can lead to gross errors in the prediction of reaction zones and induction times. Oscillations in temperature and pressure may lead to inaccurate production and destruction of radicals. The Total Variation Diminishing (TVD) approach has been taken by several investigators [25, 26, 39, 43, 44, 45, 46] to try to accurately capture shock waves and reaction fronts. Yee and Shinn [40] investigated several aspects of semi-implicit and fully implicit shock-capturing methods for reacting flow. Ju [18] used a fourth order MUSCL (Monotone Upwind Scheme for Conservation Laws) scheme with Steger–Warming flux vector splitting to calculate reactive flows. Jameson [16, 17] has presented a framework for Local Extremum Diminishing (LED) and Essentially Local Extremum Diminishing (ELED) schemes which have been shown to have excellent shock capturing qualities for non-reactive perfect gas flows. The LED/ELED framework includes the TVD concept but has the advantage of being equally generalizable to structured and unstructured grids, unlike TVD. One scheme, the Convective Upwind and Split Pressure (CUSP) scheme, has good shock capturing properties and has been shown to give accurate viscous solutions without spurious numerical dissipation [34, 35]. Because of its high accuracy in viscous dominated regions, it would be expected to provide the same accuracy in regions where species diffusion effects are present. Thus, the CUSP splitting combined with a flux limiter may be able to provide good resolution of inviscid and viscous reactive flow phenomena.

In this work, the point-implicit formulation of Bussing and Murman is combined with an explicit time-stepping multigrid solver [23] using CUSP dissipation to compute high speed reactive flows. The algorithm is implemented using the MPI standard on an IBM SP. The fully explicit nature of the point implicit scheme allows the algorithm to be implemented in a fairly straightforward manner on a parallel computing platform. Because of the compact stencil used in the underlying explicit numerical discretization, the cost of parallel communication is quite low. This attribute, combined with the large amount of computational work involved for each cell in a reactive flow simulation, leads to a highly parallel efficient algorithm [29].

2. GOVERNING EQUATIONS

The two-dimensional equations for chemically reacting flow can be written in a Cartesian coordinate system (x, y) as

$$\frac{\partial \mathbf{w}}{\partial t} + \frac{\partial (\mathbf{f} - \mathbf{f}_\mathbf{v})}{\partial x} + \frac{\partial (\mathbf{g} - \mathbf{g}_\mathbf{v})}{\partial y} = \dot{\omega}, \tag{1}$$

where $\mathbf{w}$ is the vector of flow variables, $\mathbf{f}$ and $\mathbf{g}$ are the convective flux vectors, $\mathbf{f}_\mathbf{v}$ and $\mathbf{g}_\mathbf{v}$ are the diffusive flux vectors, and $\dot{\omega}$ is the vector of source terms. Consider a control volume Ω with boundary $\partial\Omega$. The equations of motion of the fluid can then be written in integral

form as

$$\frac{d}{dt}\iint_{\Omega}\mathbf{w}\,dx\,dy+\oint_{\partial\Omega}(\mathbf{f}\,dy-\mathbf{g}\,dx)$$
$$=\oint_{\partial\Omega}(\mathbf{f}_{\mathbf{v}}\,dy-\mathbf{g}_{\mathbf{v}}\,dx)+\iint_{\Omega}\dot{\omega}\,dx\,dy, \tag{2}$$

where $\mathbf{w}$ is the vector of flow variables

$$\mathbf{w}=\begin{Bmatrix}\rho_i\\ \rho u\\ \rho v\\ \rho E\end{Bmatrix},$$

$\mathbf{f}$, $\mathbf{g}$ are the convective flux vectors

$$\mathbf{f}=\begin{Bmatrix}\rho_i u\\ \rho u^2+p\\ \rho uv\\ \rho Eu+pu\end{Bmatrix},\qquad \mathbf{g}=\begin{Bmatrix}\rho_i v\\ \rho uv\\ \rho v^2+p\\ \rho Ev+pv\end{Bmatrix},$$

$\mathbf{f}_{\mathbf{v}}$, $\mathbf{g}_{\mathbf{v}}$ are the diffusive flux vectors including species diffusion effects

$$\mathbf{f}_{\mathbf{v}}=\begin{Bmatrix}-\rho_i u_{di}\\ \tau_{xx}\\ \tau_{xy}\\ -q_x-\sum_{i=1}^{N}\rho_i u_{di}h_i+\tau_{xx}u+\tau_{xy}v\end{Bmatrix},$$

$$\mathbf{g}_{\mathbf{v}}=\begin{Bmatrix}-\rho_i v_{di}\\ \tau_{yx}\\ \tau_{yy}\\ -q_y-\sum_{i=1}^{N}\rho_i v_{di}h_i+\tau_{yx}u+\tau_{yy}v\end{Bmatrix},$$

and $\dot{\omega}$ is the chemical source vector

$$\dot{\omega}=\begin{Bmatrix}\dot{\omega}_i\\ 0\\ 0\\ 0\end{Bmatrix}.$$

In these equations, $i=1,\ldots,N$ and N is the number of species. For a thermally perfect gas, pressure may be determined from

$$p=\rho RT, \tag{3}$$

where R is the mixture gas constant. The density is found from

$$\rho=\sum_{i=1}^{N}\rho_i. \tag{4}$$

Temperature may be determined from the relation

$$E = e + \frac{1}{2}(u^2 + v^2) = \sum_{i=1}^{N} \frac{\rho_i}{\rho} h_i - \frac{p}{\rho} + \frac{1}{2}(u^2 + v^2), \tag{5}$$

where h_i are the individual species enthalpies which depend solely on temperature for a thermally perfect gas. Combining the NASA polynomial representation of species enthalpies [11] with the previous equation for energy yields an implicit equation for temperature which is solved by Newton iteration.

As a first approximation, Fick's Law is used to determine the individual species diffusion velocities:

$$\rho_i \mathbf{u}_{di} = -\rho D_i \nabla \left(\frac{\rho_i}{\rho} \right). \tag{6}$$

The diffusion coefficient D_i is determined from the formulation following Williams [37] such that

$$D_i = \frac{1 - X_i}{\sum_{j \neq i} (X_j / D_{ij})}, \tag{7}$$

where X_i is the mole fraction of species i and D_{ij} is the binary diffusion coefficient between species i and j. The mixture viscosity and thermal conductivity are obtained in a mixture-averaged manner [19].

3. CHEMICAL MODEL

One strength of the current work is that the resulting code can use an arbitrary chemical model, thus allowing for quick comparison of reaction sets. Therefore, several different chemistry models for hydrogen/air combustion are used in this work. The first is a reduced equation model for hydrogen/air combustion due to Evans and Schexnayder [9] involving seven species and eight reactions. Nitrogen in this set is treated as an inert diluent. The second group of rate equations is the nine species, nineteen reaction modified model of Jachimowski [13] and Wilson and MacCormack [38]. Again, nitrogen is treated as an inert diluent because reactions involving nitrogen have been determined to be negligible below Mach 5 [26]. Another chemistry model is that of Yetter *et al.* [20, 41, 42]. This mechanism, which is part of a broader mechanism for the $CO/H_2O/O_2$ system, contains eight reacting species and 21 reactions. The last model was one proposed by Westbrook [36] which includes eight reacting species and seventeen reactions for hydrogen/oxygen combustion.

The chemical source terms are computed in the Arrhenius form, with the forward rate coefficients, k_{fj}, given by

$$k_{f_j} = A_j T^{n_j} \exp\left(\frac{-E_{Aj}}{\mathcal{R}T} \right), \tag{8}$$

where E_{Aj} is the activation energy of the jth forward reaction. The reverse rate coefficients are evaluated using the equilibrium constant for concentration

$$K_{c_j} = \frac{k_{f_j}}{k_{b_j}}. \tag{9}$$

This concentration equilibrium constant is obtained from the equilibrium constant in terms

of partial pressures,

$$K_{c_j} = K_{p_j} \left(\frac{P_{atm}}{\mathcal{R}T} \right)^{\sum_{i=1}^{N} \nu_{ij}}, \tag{10}$$

where N is the number of species and ν_{ij} is the change in the number of moles of species i in reaction j. The equilibrium constant K_{p_j} is calculated from the standard Gibbs free energy change for each reaction. Standard state free energies are obtained from the NASA polynomial set [11].

4. NUMERICAL MODEL

4.1. *Flow Equations*

The governing equations are solved using a conservative second-order accurate finite volume formulation in which the chemical source terms are treated point implicitly.

When the integral governing equations (2) are independently applied to each cell i, j in the domain, we obtain a set of coupled ordinary differential equations of the form

$$\frac{d}{dt}(\mathbf{w}_{ij})V_{ij} + \mathbf{C}(\mathbf{w}_{ij}) - \mathbf{NS}(\mathbf{w}_{ij}) - \mathbf{D}(\mathbf{w}_{ij}) = \dot{\omega} V_{ij}, \tag{11}$$

where $\mathbf{C}(\mathbf{w}_{ij})$ are the convective Euler fluxes, $\mathbf{NS}(\mathbf{w}_{ij})$ are the diffusive fluxes, $\mathbf{D}(\mathbf{w}_{ij})$ are the numerical dissipation fluxes added for numerical stability reasons, and $\dot{\omega} V_{ij}$ are the chemical source terms. This Eq. (11) can be rewritten as (drop the i, j subscripts for clarity)

$$\frac{d}{dt}[\mathbf{w}]V + \mathbf{R}(\mathbf{w}) = \dot{\omega} V, \tag{12}$$

where $\mathbf{R}$ is the sum of the three flux contributions. We may further simplify this expression by defining a modified residual $\mathbf{R}'(\mathbf{w}) = \mathbf{R}(\mathbf{w}) - \dot{\omega} V$ so that our set of coupled ordinary differential equations becomes

$$\frac{d}{dt}[\mathbf{w}]V = -\mathbf{R}'(\mathbf{w}). \tag{13}$$

The governing ordinary differential equations are solved using a standard five-stage time stepping scheme [24].

4.2. *Chemical Source Terms*

The chemical source vector $\dot{\omega}$ was treated in a point implicit manner [3]. The point implicit treatment reduces the stiffness of the problem by effectively rescaling the characteristic time of the reactions so that their magnitudes are commensurate with the convective characteristic time. We begin by writing the governing ordinary differential equation for cell i, j but instead evaluate the chemical source vector at the next time level:

$$\frac{d}{dt}[\mathbf{w}]V + \mathbf{R}(\mathbf{w}^n) = \dot{\omega}^{n+1} V. \tag{14}$$

We then linearize the chemical source vector about the present time level so that

$$\dot{\omega}^{n+1} \approx \dot{\omega}^n + \frac{\partial \dot{\omega}^n}{\partial \mathbf{w}} \frac{d}{dt}[\mathbf{w}]\Delta t. \tag{15}$$

Substituting this into the governing equation and rearranging yields

$$\frac{d}{dt}[\mathbf{w}]V = \left[\mathbf{I} - \Delta t \frac{\partial \dot{\omega}^n}{\partial \mathbf{w}}\right]^{-1} [\dot{\omega}^n V - \mathbf{R}(\mathbf{w}^n)], \tag{16}$$

which is evaluated entirely at the current time level and is thus fully explicit.

This treatment necessitates the inversion of the source term Jacobian matrix with dimension $N \times N$ where N is the number of species present in the flow. An inversion for the momentum and energy equations is not necessary due to the absence of chemical source terms in those equations. This $N \times N$ inversion is done only during the first stage of each time step of the solver and is retained and used for the succeeding four stages. This time-saving step has no effect on the results of the computation.

Because the chemical source terms have been treated implicitly, the time step limitation of the explicit time integration scheme depends solely on the spectral radius of the flux Jacobian.

4.3. *Numerical Dissipation*

The Convective Upwind and Split Pressure (CUSP) scheme provides excellent resolution of shocks at high Mach numbers at a reasonable computational cost [16, 17]. CUSP has been shown to be an accurate and effective dissipation scheme for viscous flows [34] and high speed reactive flows [29, 30, 31].

For simplicity, let us work in one dimension; extension to higher dimensions is straightforward. If the flow is locally supersonic, simple upwinding is a natural choice. We consider the convective flux and pressure

$$\mathbf{f}_c = u \begin{Bmatrix} \rho_i \\ \rho u \\ \rho H \end{Bmatrix} = u\mathbf{w}_c, \qquad \mathbf{f}_p = \begin{Bmatrix} 0 \\ p \\ 0 \end{Bmatrix} \tag{17}$$

separately. Upwinding of the convective flux is achieved by

$$\mathbf{d}_{c_{j+\frac{1}{2}}} = \left|u_{j+\frac{1}{2}}\right| \Delta \mathbf{w}_{c_{j+\frac{1}{2}}} = |M| c_{j+\frac{1}{2}} \Delta \mathbf{w}_{c_{j+\frac{1}{2}}}, \tag{18}$$

where M is the local Mach number attributed to the interval. Upwinding of the pressure is achieved by

$$\mathbf{d}_{p_{j+\frac{1}{2}}} = \operatorname{sign}(M) \begin{Bmatrix} 0 \\ \Delta p_{j+\frac{1}{2}} \\ 0 \end{Bmatrix}. \tag{19}$$

Full upwinding of both $\mathbf{f}_c$ and $\mathbf{f}_p$ is incompatible with stability in subsonic flow, since pressure waves with the speed $u - c$ would be traveling backwards, and the discrete scheme would not have a proper zone of dependence. Since the eigenvalues of $\frac{\partial \mathbf{f}_c}{\partial \mathbf{w}}$ are non-negative, while those of $\frac{\partial \mathbf{f}_p}{\partial \mathbf{w}}$ are non-positive, a split with

$$\mathbf{f}^+ = \mathbf{f}_c, \qquad \mathbf{f}^- = \mathbf{f}_p \tag{20}$$

leads to a stable scheme, similar to that used by Denton [5], in which downwind differencing is used for the pressure.

This scheme does not reflect the true zone of dependence in supersonic flow. Thus one may seek a scheme with

$$\mathbf{d}_{c_{j+\frac{1}{2}}} = f_1(M) c_{j+\frac{1}{2}} \Delta \mathbf{w}_{c_{j+\frac{1}{2}}} \tag{21}$$

$$\mathbf{d}_{p_{j+\frac{1}{2}}} = f_2(M) \begin{Bmatrix} 0 \\ \Delta p_{j+\frac{1}{2}} \\ 0 \end{Bmatrix}, \tag{22}$$

where $f_1(M)$ and $f_2(M)$ are blending functions with the asymptotic behavior $f_1(M) \to |M|$ and $f_2(M) \to \text{sign}(M)$ for $|M| > 1$. Also the convective diffusion should remain positive when $M = 0$, while the pressure diffusion must be antisymmetric with respect to M. A simple choice is to take $f_1(M) = |M|$ and $f_2(M) = \text{sign}(M)$ for $|M| > 1$, and to introduce blending polynomials in M for $|M| < 1$ which merge smoothly into the supersonic segments. A quartic formula

$$f_1(M) = a_o + a_2 M^2 + a_4 M^4, \qquad |M| < 1 \tag{23}$$

preserves continuity of f_1 and $\frac{df_1}{dM}$ at $|M| = 1$ if

$$a_2 = \frac{3}{2} - 2a_o, \qquad a_4 = a_o - \frac{1}{2}. \tag{24}$$

Then a_o controls the diffusion at $M = 0$. For transonic flow calculations a good choice is $a_o = \frac{1}{4}$, while for very high speed flows it may be increased to $\frac{1}{2}$. A suitable blending formula for the pressure diffusion is

$$f_2(M) = \frac{1}{2} M(3 - M^2), \qquad |M| < 1. \tag{25}$$

This splitting can be shown to be approximately equivalent [16] to the Liou–Steffen splitting [22]. The final form of the diffusive flux for cell interface $j + \frac{1}{2}$ is

$$\mathbf{d}_{j+\frac{1}{2}} = \mathbf{d}_{c_{j+\frac{1}{2}}} + \mathbf{d}_{p_{j+\frac{1}{2}}}. \tag{26}$$

In the case of viscous flows, the spectral radius used for the dissipation is reduced by the spectral radius of the diffusive fluxes so that artificial diffusion does not swamp the physical diffusion present in the flow.

4.4. *Flux Limiting*

The CUSP splitting by itself will achieve a first order diffusive flux and thus will cause the numerical solution to remain monotone in regions of high gradients. To recover the second order accuracy of the finite volume scheme in smooth regions, we use a flux limiter.

The limiter is used in the following way. Define the modified diffusive flux, $d'_{i+1/2}$ for the jth equation as

$$d'_{i+\frac{1}{2}} = d_{i+\frac{1}{2}} - L\left(d_{i+\frac{3}{2}}, d_{i-\frac{1}{2}}\right), \tag{27}$$

where L is a limiter that has the properties of an average, except that $L(u, v) = 0$ if u and v have opposite signs. We can see that if an extremum exists in either cell i or cell $i + 1$, then

the limiter will have a value of zero, thus enforcing a first order diffusive flux and forcing the solution toward monotonicity. If an odd-even mode develops, then the limiter will be non-zero, effectively adding third order dissipation to damp the odd-even mode. Otherwise, the limiter will effectively add anti-diffusion to the first order diffusive flux, allowing the scheme to retain its second order accuracy.

A symmetric positive limiter that was applied in this work was the α-mean limiter,

$$L\left(d_{i+\frac{3}{2}}, d_{i-\frac{1}{2}}\right) = \alpha S\left(d_{i+\frac{3}{2}}, d_{i-\frac{1}{2}}\right) \min(A, B, C), \tag{28}$$

where

$$S(u, v) = \frac{1}{2}\{\text{sign}(u) + \text{sign}(v)\} \tag{29}$$

$$A = \left|d_{i+\frac{3}{2}}\right| \tag{30}$$

$$B = \left|d_{i-\frac{1}{2}}\right| \tag{31}$$

$$C = \frac{1}{2}\left|d_{i+\frac{3}{2}} + d_{i-\frac{1}{2}}\right|. \tag{32}$$

This limiter has the disadvantage of being active near smooth extrema and will force the scheme to be first order accurate in that neighborhood.

A way to overcome this limitation is to construct a limiter which becomes local extremum diminishing for the scalar case as the mesh spacing approaches zero (Essentially Local Extremum Diminishing). This limiter can be constructed by setting

$$L(u, v) = \frac{1}{2} D(u, v)(u + v), \tag{33}$$

where

$$D(u, v) = 1 - \left|\frac{u - v}{\max(|u| + |v|, \epsilon \Delta x^r)}\right|^q, \tag{34}$$

where $r = \frac{3}{2}$, $q \geq 2$, and $\epsilon > 0$ is a small number. Then, if $D(u, v)$ is applied in the neighborhood of a smooth extremum, the dissipative flux will be of order Δx^2 [16]. In this work, both the LED and ELED limiters described above were implemented and tested for both inviscid and viscous reactive flows. The differences between the results using each limiter were minimal and thus the LED and ELED limiters were used interchangeably.

The final form of the artificial diffusive flux is then

$$\mathbf{D}(\mathbf{w}_{ij}) = \mathbf{d}'_{i+\frac{1}{2},j} - \mathbf{d}'_{i-\frac{1}{2},j} + \mathbf{d}'_{i,j+\frac{1}{2}} - \mathbf{d}'_{i,j-\frac{1}{2}}. \tag{35}$$

4.5. *Boundary Conditions*

The surface boundary is modeled as an adiabatic, non-catalytic inert surface. For Euler calculations, flow tangency is enforced at the surface while a no-slip boundary condition is used for viscous flows. Due to the supersonic nature of the flow, outflow boundary quantities are extrapolated from the interior and inflow quantities are taken to be free stream values.

Free stream values of radical species are set to a mass fraction of 1×10^{-11}. Varying this value did not affect the results.

5. MULTIGRID CONVERGENCE ACCELERATION

Multigrid acceleration has been applied quite successfully to the solution of both the non-reactive Euler and Navier–Stokes equations [23, 24, 34]. However, the application of multigrid methods to reactive flow calculations has been limited. Bussing and Murman [3] reported success in using Ni's multigrid method for one-dimensional reactive flow calculations. Additional examples of multigrid acceleration for reactive flows are lacking.

The approach taken in this paper is to use a previously validated multigrid solver [23, 24, 34] and include chemical source terms on all levels [29, 30]. The coarse grid corrections to the species densities are limited to ensure that no mass fraction becomes negative. Varying degrees of underrelaxation can be used to enhance the convergence rate while capturing the sharp gradients and large radical growth regions that characterize reactive flow problems.

The multigrid scheme is a full approximation scheme defined as follows [14, 15]. Denote the grids by a subscript k. Start with a time step on the finest grid $k = 1$. Transfer the solution from a given grid to a coarser grid by a transfer operator $P_{k,k-1}$, so that the initial state on grid k is

$$\mathbf{w}_k^{(0)} = P_{k,k-1}\mathbf{w}_{k-1}. \tag{36}$$

This transfer operation is done in a manner to be fully conservative

$$\mathbf{w}_k^{(0)} = \frac{\sum_{ij} \mathbf{w}_{k-1} V_{ij}}{\sum_{ij} V_{ij}}. \tag{37}$$

Then on grid k the multistage time stepping scheme is reformulated as

$$\mathbf{w}_k^{(q+1)} = \mathbf{w}_k^{(0)} - \alpha_{q+1}\Delta t\left(\mathbf{R}_k'^{(q)} + \mathbf{G}_k\right), \tag{38}$$

where the residual $\mathbf{R}_k'^{(q)}$ is evaluated from current and previous values, and the forcing function $\mathbf{G}_k$ is defined as the difference between the aggregated residuals transferred from grid $k-1$ and the initial residual calculated on grid k. Thus

$$\mathbf{G}_k = \theta_u Q_{k,k-1}\mathbf{R}'(\mathbf{w}_{k-1}) - \mathbf{R}'\left(\mathbf{w}_k^{(0)}\right), \tag{39}$$

where $Q_{k,k-1}$ is another transfer operator which collects the residuals in a conservative manner. The constant θ_u is an underrelaxation factor, intended to be used to avoid instabilities caused by collected chemical source terms on the fine grid forcing the coarse grid solution in a spurious manner. Because only the fine grid may have sufficient resolution to capture induction and reaction zones, forcing by the full collected residual may cause an unphysical broadening of heat release regions, leading to instabilities on the coarse grid. This effect may also limit the number of multigrid levels which can be used for a given fine grid resolution. The distribution of mesh points in the grids used for our computations allowed the testing of the scheme using only two levels of multigrid. Typical values for the scalar θ_u range from 0.75 to 1.00. During the first stage on the coarse grid, the forcing term $\mathbf{G}_k$ simply replaces the coarse grid residual by the aggregated fine grid residuals

$$\mathbf{w}_k^{(1)} = \mathbf{w}_k^{(0)} - \alpha_1\Delta t\left(\theta_u Q_{k,k-1}\mathbf{R}'(\mathbf{w}_{k-1})\right), \tag{40}$$

so that the coarse grid is forced by some portion of the fine grid solution. The solution is then advanced in the usual manner on the coarse grid. The accumulated correction on a

coarser grid is transferred to the next higher grid by a limited interpolation operator $I'_{k-1,k}$ so that the solution on grid $k-1$ is updated by the formula

$$\mathbf{w}_{k-1}^{new} = \mathbf{w}_{k-1} + I'_{k-1,k}\left(\mathbf{w}_k - \mathbf{w}_k^{(0)}\right). \tag{41}$$

The limited interpolation operator has the usual properties of a bilinear interpolant in addition to a filter which prevents individual species densities on the fine grid from being updated to a negative density. This simple limiter consists of a logic check on the updated species density; if the updated value will become negative, a smaller portion of the coarse grid correction is added to the fine grid solution. The whole set of grids is traversed in a W-cycle in which time steps are only performed when moving down the cycle. First order numerical diffusion is always used on the coarse grids because only the interpolated corrections are added to the fine grid variables. The use of a higher order scheme on the coarser levels has been observed to lead to a loss of robustness. In addition, using first order dissipation saves computational time and helps damp out error modes more quickly as well.

6. RESULTS AND DISCUSSION

The formulation described in this work was applied to non-reactive and reactive flows in order to verify and validate the algorithm. Reference [29] presents several test cases involving inviscid and diffusive non-reactive and reactive flows with analytic or asymptotic solutions. In this article, both inviscid axisymmetric flows over spherical blunt bodies and two-dimensional viscous ramp flows using detailed chemical models for hydrogen combustion are considered.

The MPI standard is used to parallelize the code on an IBM SP. A static domain decomposition with two-level halos for flow quantities and one-level halos for grid information is used. The current point implicit scheme will achieve a higher level of speedup as compared to a convective flow code alone due to the larger number of operations that take place per cell [29, 31].

Figure 1 shows a typical parallel speedup for this algorithm for an inviscid reactive simulation on a 64×64 cell mesh. As expected, efficiency decreases with the number of processors due to communication overhead. This relatively small grid achieves quite respectable parallel efficiencies, testifying to the high efficiencies attainable by explicit algorithms for reactive flows. This indicates that the algorithm should scale reasonably well, so that increasing the resolution of the grid while using a larger number of processors will take approximately the same amount of wallclock time. Reactive simulations including diffusive effects would be expected to be at least as parallel efficient as this inviscid simulation. This is due to the increased amount of computational work necessary for diffusive simulations while communication costs would remain approximately the same.

Stoichiometric hydrogen/oxygen flow over an axisymmetric spherical tip projectile at $M = 3.55$ was simulated using the reduced chemistry model (six species, eight reactions) of Evans and Schexnayder [9]. This corresponds to an experiment conducted by Lehr [21]. The diameter of this projectile is 15 mm. The free stream temperature is 292 K and the free stream pressure is 24,800 Pa. The grid in this case is 64×64 cells. The bow shock in front of the body raises the temperature of the flow so that, after an induction zone, the flow reacts. As shown in Fig. 2, the length of the induction zone varies depending on the post shock temperature which corresponds to the relative strength of the shock. Temperature is

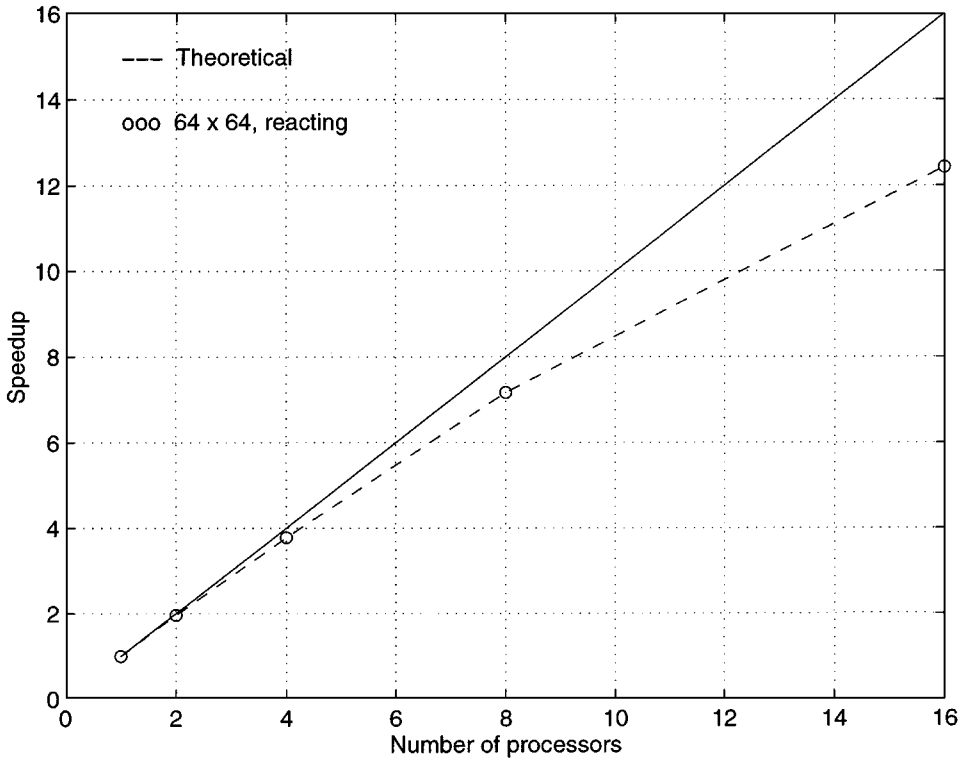

FIG. 1. Parallel speedup for inviscid reacting case.

approximately constant in the induction zone as radicals build up to the necessary levels to react and produce water vapor. The production of water vapor is accompanied by heat release which raises the temperature and, because pressure is nearly constant across the reaction zone, lowers the density. Figure 3 shows the temperature along the stagnation streamline computed using the Evans and Schexnayder reaction model and also the Jachimowski eight species, nineteen reaction modified model. The eight species, nineteen reaction model produced a slightly different shock location, while the point of heat release is close to the Evans and Schexnayder model. The only difference between these two calculations was the chemistry model used: both models used the same algorithm and grid and were converged to the same level of accuracy. Thus, even though both simulations are converged, different solutions result because the mathematical models were slightly different in the modeling of the chemistry. The difference in shock location could be explained by a difference in relaxation characteristics behind the shock due to the chemical models. In addition, the heat release profiles lead to slightly different static pressures behind the heat release region, which could result in different shock positions. Figure 3 indicates that the numerical dissipation scheme is providing the necessary dissipation in regions of steep gradients, such as the shock, to prevent oscillations and preserve monotonicity while still allowing sharp resolution.

However, upon examining Fig. 2, one may notice that the numerical solution differs slightly from the experimental shock location and heat release front. Thus, another simulation was performed on a 64×128 cell grid which had twice the number of grid cells in the normal direction as the 64×64 grid had. The Evans and Schexnayder model was used for the chemistry, since it produced a shock location that was closer to the body on the

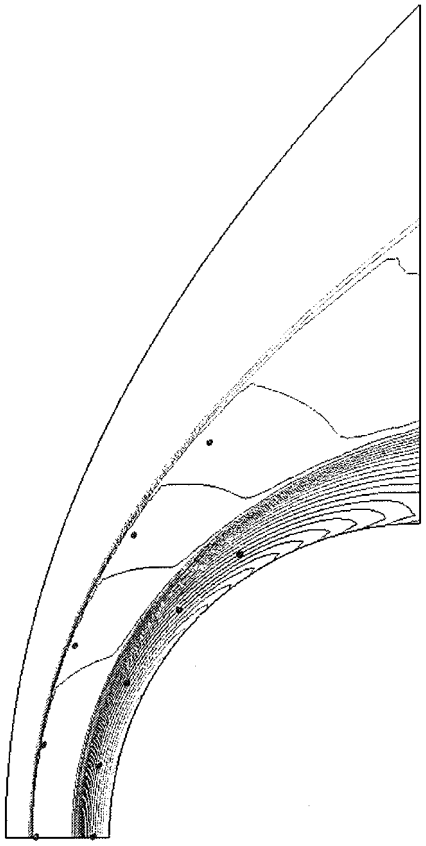

FIG. 2. Temperature contours: $M = 3.55$ hydrogen/oxygen. Contour levels in K: min, 250; max, 3130; inc, 93. Grid size, 64×64. Circles indicate experimental shock and heat release locations.

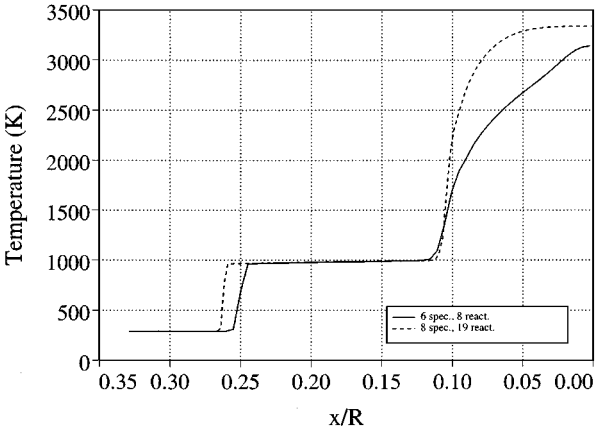

FIG. 3. Temperature along stagnation streamline for two different chemical models: $M = 3.55$ hydrogen/oxygen; projectile surface at $x/R = 0.00$. Grid size, 64×64.

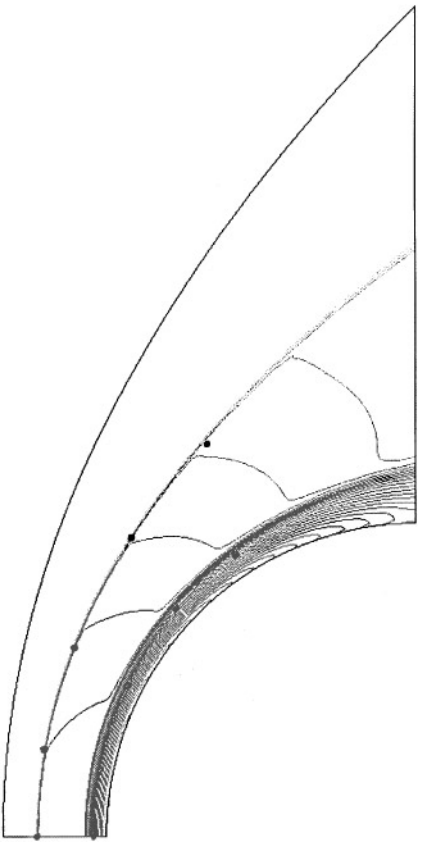

FIG. 4. Temperature contours: $M = 3.55$ hydrogen/oxygen. Contour levels in K: min, 250; max, 3130; inc, 93. Grid size, 64×128. Circles indicate experimental shock and heat release locations.

64×64 grid. Temperature contours for this finer grid simulation are presented in Fig. 4 along with experimental shock and heat release front locations. As can be seen, the agreement between the experimental results and the numerical simulation is much better on this finer grid. The increased resolution has moved the shock closer to the body, increased the length of the induction zone, and moved the heat release front closer to the body. Density and pressure contours are presented in Figs. 5 and 6.

The temperature along the stagnation streamline for the 64×128 grid is shown in Fig. 7. As in the case of the 64×64 cell grid, the flow passes through a shock which is followed by an induction zone where radicals are created due to the higher temperature. After sufficient amounts of radicals have been formed, water vapor is created, increasing the temperature and further hastening the reaction.

The mass fractions of the reactants and products for the Evans model simulation on the 64×128 grid are plotted in Fig. 8. As expected, the reactants have almost constant mass fraction through the shock and only begin to be consumed in the heat release region. Water vapor is not formed in any appreciable quantity until the heat release region. It should also be noted that the mass fraction profiles are monotonic; no overshoots in the mass fraction of these primary components is observed, again indicating good performance of the CUSP dissipation scheme.

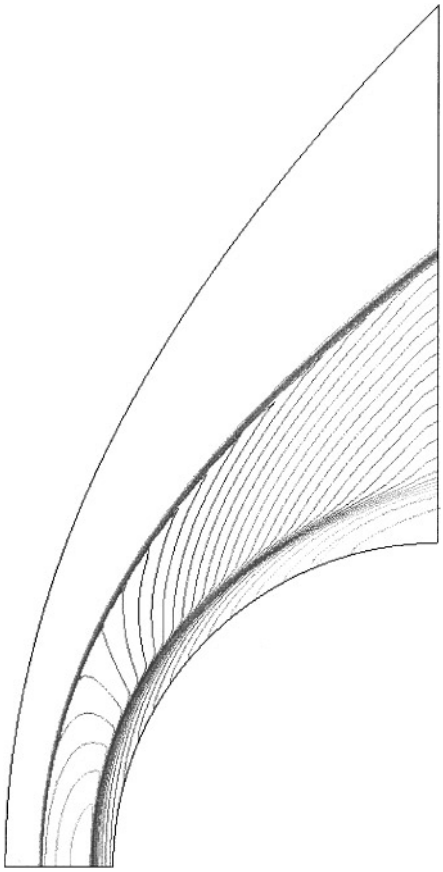

FIG. 5. Density contours: $M = 3.55$ hydrogen/oxygen. Contour levels in kg/m^3: min, 0.05; max, 0.6; inc, 0.016. Grid size, 64×128.

The growth and destruction of radical species is depicted in Fig. 9 for the Evans model. This figure shows the logarithm of the mass fractions of the radical species. Exponential growth can be observed in the induction zone, which is to be expected. After a small region of slow growth, the radical mass fractions grow approximately nine orders of magnitude in a very short distance, which is a testament to the ability of the CUSP splitting and the flux limiter to capture large changes in the conservative variables without oscillation and without undue damping. The mass fraction of the radicals does not decrease greatly after the heat release zone, even with the formation of a great deal of water vapor. This is due to the conversion of the reactants into radical species which then combine directly to form water.

Upon examination of Fig. 4, it can be seen that the agreement between the computation and experiment is quite good. This computation also agrees favorably with the simulation of Yungster *et al.* [45] who limited the cell Damköhler number so that the heat release was spread out among two to three cells. Because of the point implicit treatment of the chemical model, no such limitation is necessary using the current formulation.

Figures 10 and 11 show the convergence histories for the six species, eight reaction 64×64 cell calculation without and with multigrid acceleration. The convergence histories present the root mean squared residual of the density of water and the number of supersonic

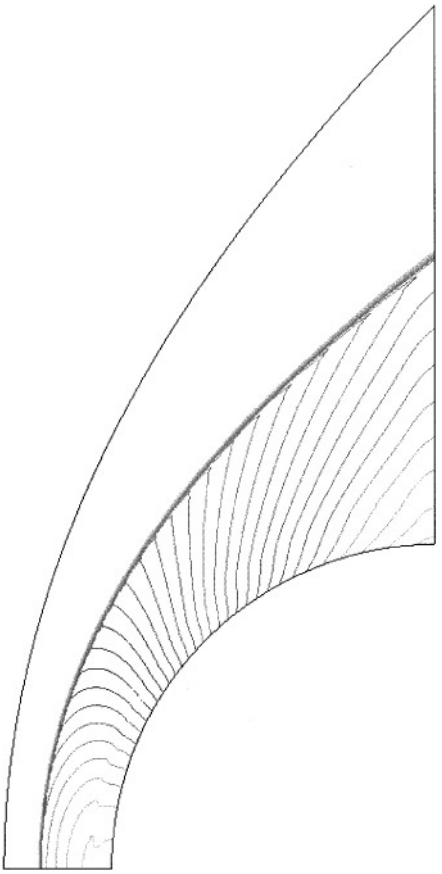

FIG. 6. Normalized pressure contours: $M = 3.55$ hydrogen/oxygen. Contour levels (p/p_∞): min, 1.0; max, 16.5; inc, 0.5. Grid size, 64×128.

cells in the domain versus the number of cycles. The initial increase in the density residual is due to the production of water as the flow initially reacts and the bow shock and reaction zone move outward from the body. The use of multigrid provides a significant convergence acceleration in this problem without compromising the accuracy of the solution.

The single grid calculation converged about six orders of magnitude in 2000 iterations, consuming 995 seconds (wall clock) using four processors of an IBM SP. The multigrid calculation, using only two levels of multigrid for this 64×64 mesh, converged fourteen orders of magnitude in 2000 iterations while requiring 1250 seconds on four processors. The same level of convergence (which results in a solution that does not change) as the single grid case using multigrid takes about 800 iterations at a cost of 500 seconds, almost halving the computational time. The converged solutions with and without multigrid acceleration are virtually identical due to the correct forcing of the coarse grid by the fine grid solution. No unphysical diffusion of radical species is seen. The convergence history for the multigrid 64×128 cell simulation is shown in Fig. 12. Multigrid again provides a significant convergence acceleration.

A two dimensional viscous reactive test case was taken from an experiment performed by Fielding [10]. In this experiment (Fig. 13), a wedge of half angle 6.34° was placed in a free stream of partially reacted hydrogen and air. The free stream Mach number was 2.10, the

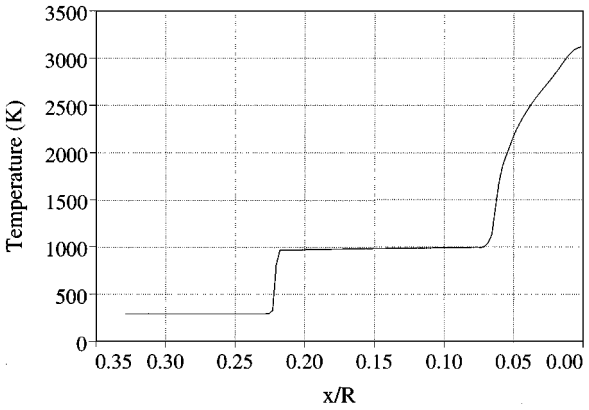

FIG. 7. Temperature along stagnation streamline: $M = 3.55$ hydrogen/oxygen; projectile surface at $x/R = 0.00$. Grid size, 64×128.

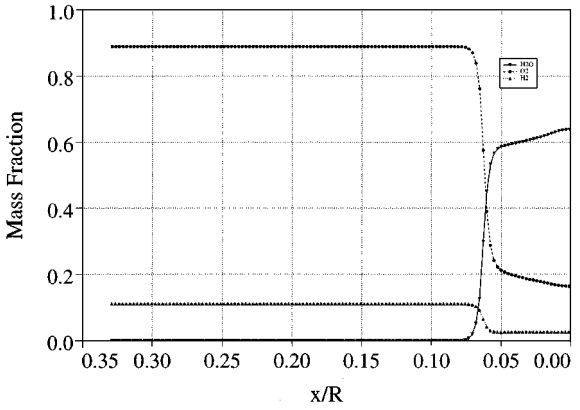

FIG. 8. Mass fractions along stagnation streamline: $M = 3.55$ hydrogen/oxygen. Shock location is at $x/R = 0.22$; heat release region begins at $x/R = 0.065$; projectile surface at $x/R = 0.00$. Grid size, 64×128. ▼ = H_2O; ● = O_2; ▲ = H_2.

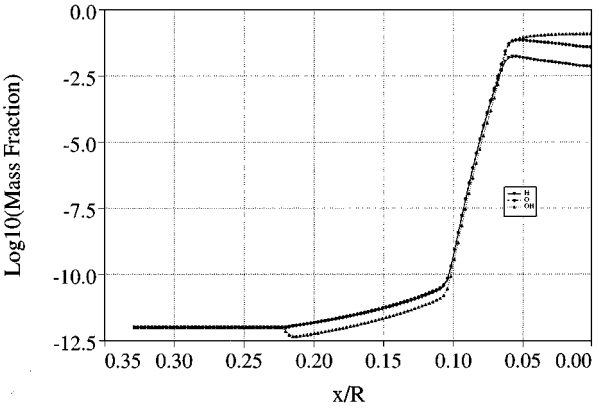

FIG. 9. Logarithm of radical mass fractions along stagnation streamline: $M = 3.55$ hydrogen/oxygen. Shock location is at $x/R = 0.22$; heat release region begins at $x/R = 0.065$; projectile surface at $x/R = 0.00$. Grid size, 64×128. ▼ = H; ● = O; ▲ = OH.

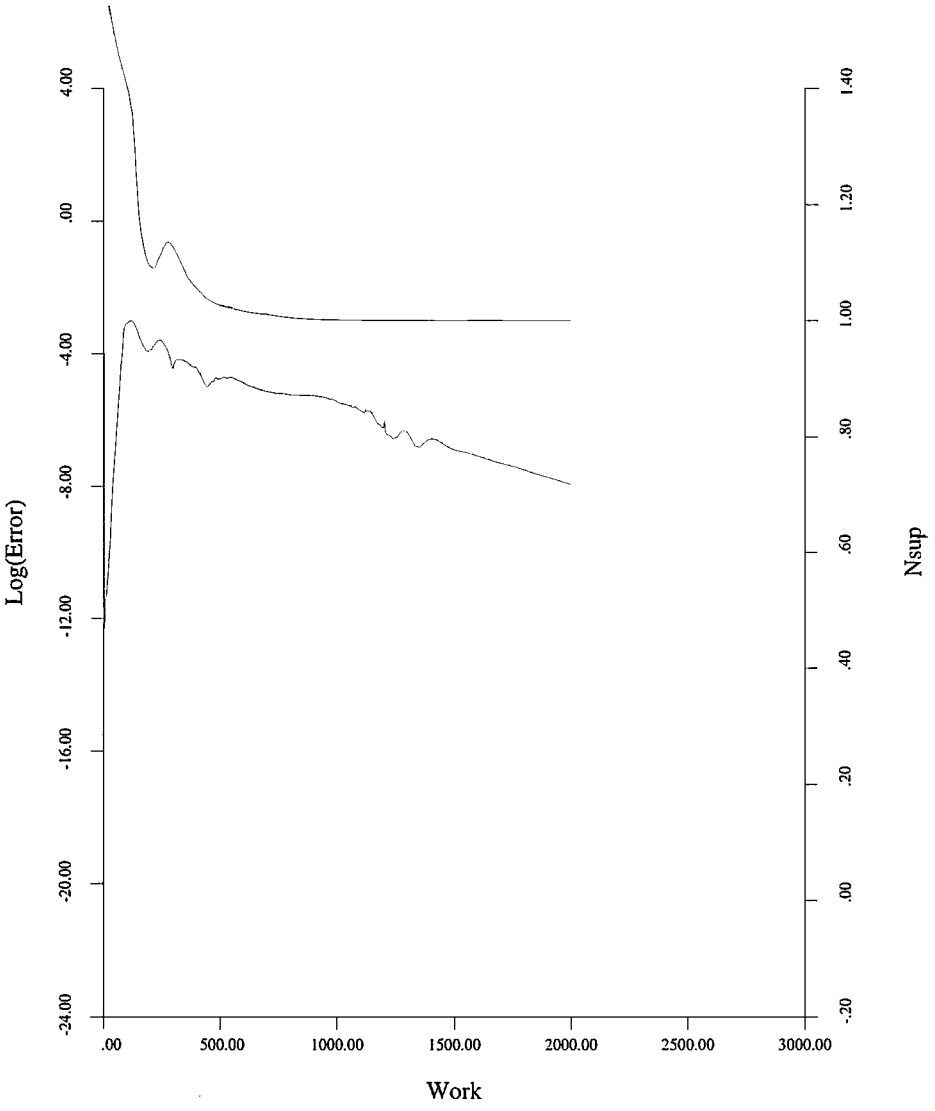

FIG. 10. Single grid convergence history: $M = 3.55$ hydrogen/oxygen. Grid size, 64×64.

free stream temperature was approximately 569 K, and the pressure was 0.060 atmospheres. The object of the experiment was to see if radical-seeded hydrogen/air mixtures would react at low pressures over a wedge after passing through an oblique shock. The mass fractions of the inlet flow were determined by Fielding using a one dimensional reacting gas code and are given in Table 1. Hydrogen had been injected into the air stream upstream of the ramp, partially reacted, and then expanded so that the flow constituents became frozen. It was assumed that nitrogen was an inert diluent. Due to the low pressure, the Reynolds number at the end of the ramp is approximately 33,000 so that fully laminar flow may be assumed. A laminar Prandtl number of 0.725 was assumed, so that the Pèclet number was approximately 23,900 at the end of the ramp. Species diffusion and heat conduction effects are included in the simulation. The nine species, 21 reaction model of Yetter *et al.* was used because it had been the model utilized to generate the composition of the incoming flow.

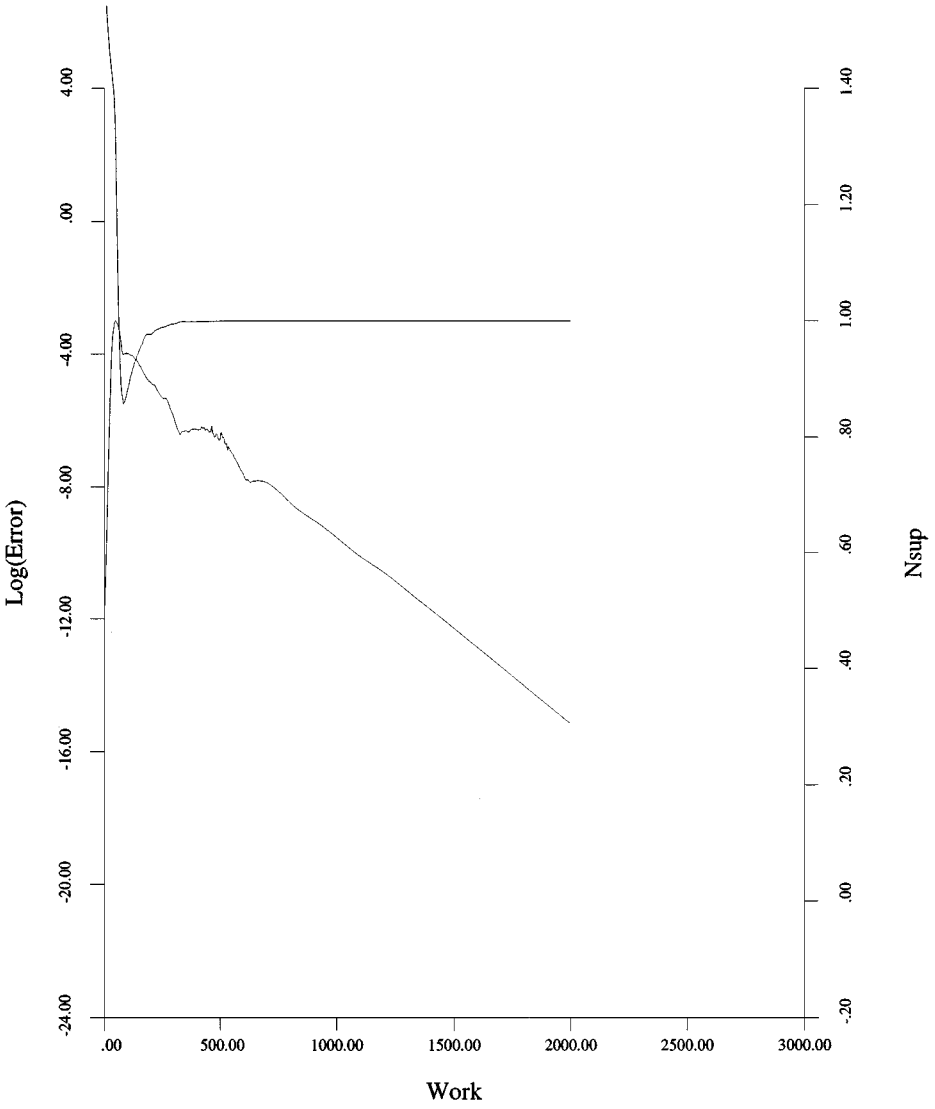

FIG. 11. Multigrid convergence history: $M = 3.55$ hydrogen/oxygen. Grid size, 64×64.

The flow was simulated on a grid with 128 cells in the streamwise direction and 96 in the direction normal to the plate. Symmetry boundary conditions were implemented along the centerline of the flow upstream of the wedge so that the governing equations were solved on only half of the experimental domain. The grid was clustered near the leading edge of the wedge to properly resolve the growth of the boundary layer and the shock attachment. Cells were also clustered near the ramp to resolve the boundary layer structure adequately; approximately 32 cells were within the boundary layer.

Figure 14 presents contours of density for this flow. The relatively thick boundary layer is immediately noticeable. Because of this thick boundary layer, the shock near the leading edge of the plate is at a much higher angle than the region away from the ramp. The growing displacement thickness from the boundary layer causes the main flow to see an effectively curved wall and thus, weak expansion waves are formed to adjust the curvature of the shock.

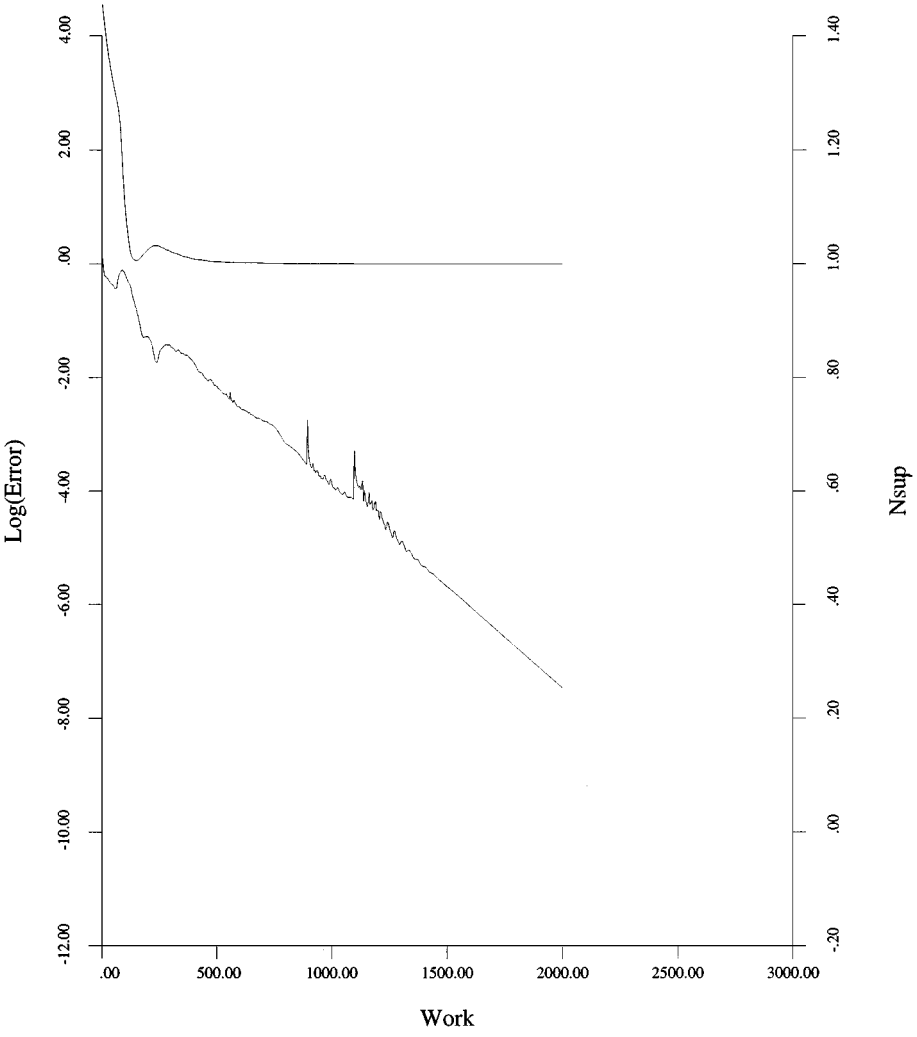

FIG. 12. Multigrid convergence history: $M = 3.55$ hydrogen/oxygen. Grid size, 64×128.

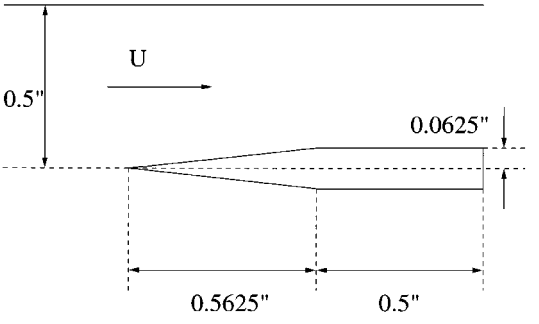

FIG. 13. Experimental setup for $M = 2.10$ viscous wedge.

TABLE 1
Free Stream Mass Fractions for $M = 2.10$ Hydrogen/Air Viscous Wedge Flow

Species	Mass Fraction
H_2	6.86×10^{-3}
O_2	1.75×10^{-1}
H_2O	2.86×10^{-2}
N_2	7.84×10^{-1}
H	2.33×10^{-4}
O	9.66×10^{-4}
OH	1.65×10^{-4}
HO_2	3.97×10^{-3}
H_2O_2	4.76×10^{-10}

It is also important to point out the absence of large heat release regions even though the domain near the leading edge experiences a relatively large compression. The shock angle obtained from the numerical simulation is 35.0° while the experimental shock angle is 34.5°. The pressure field (Fig. 15) yields trends similar to the density field. There is curvature of the shock near the leading edge and expansion waves may be seen in the region behind the oblique shock. Very little change in the pressure is seen through the boundary layer.

The lack of progress of the reaction may be understood by viewing Fig. 16, which shows contours of the logarithm of OH mass fraction. It is immediately obvious that the inlet mass fractions are not in an equilibrium state, as rapid reaction takes place in the free stream flow,

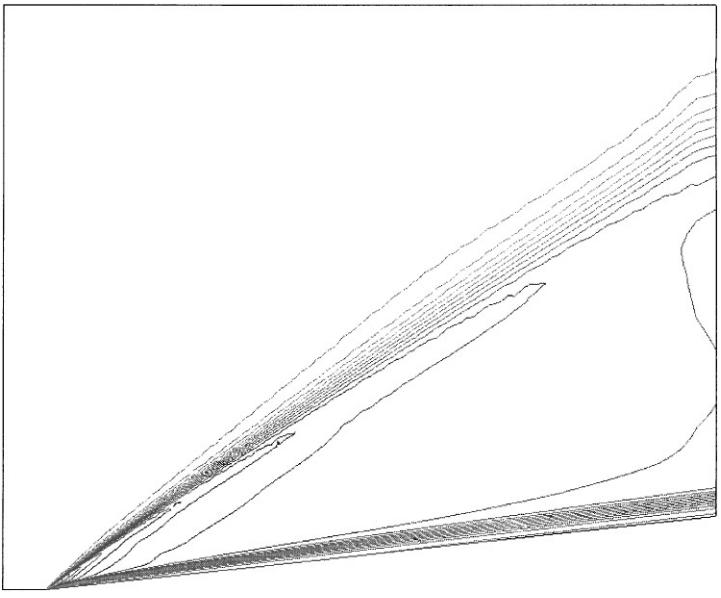

FIG. 14. Density contours: $M = 2.10$ hydrogen/air 6.34° viscous ramp. Contour levels in kg/m^3: min, 0.033; max, 0.056; inc, 0.00129.

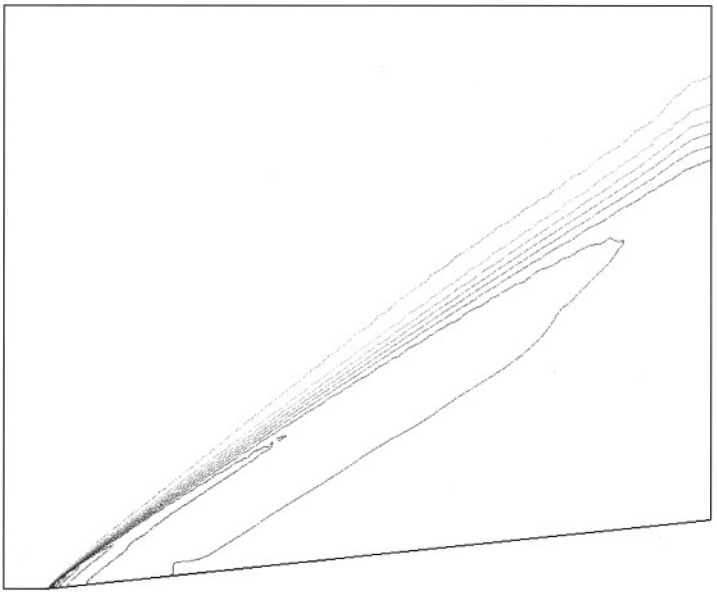

FIG. 15. Normalized pressure contours: $M = 2.10$ hydrogen/air 6.34° viscous ramp. Contour levels (p/p_∞): min, 1.0; max, 3.06; inc, 0.0857.

producing more OH. Behind the shock, the increased pressure and temperature and slightly increased residence time cause faster formation of OH, but the post shock temperature and pressures are not sufficient to allow large quantities of OH to strip hydrogen atoms from H_2 molecules and form water vapor. Near the ramp surface, it can be observed that some

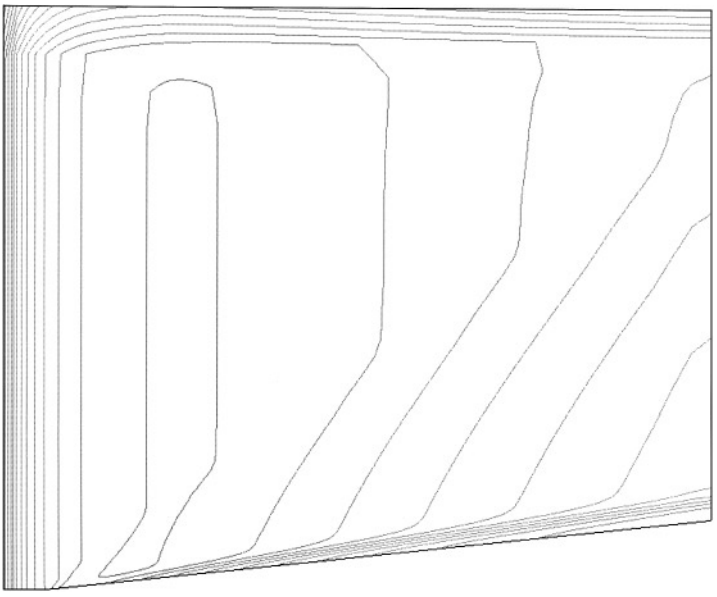

FIG. 16. Logarithm of OH mass fraction contours: $M = 2.10$ hydrogen/air 6.34° viscous ramp. Contour levels: min, -3.33; max, -2.65; inc, 0.057.

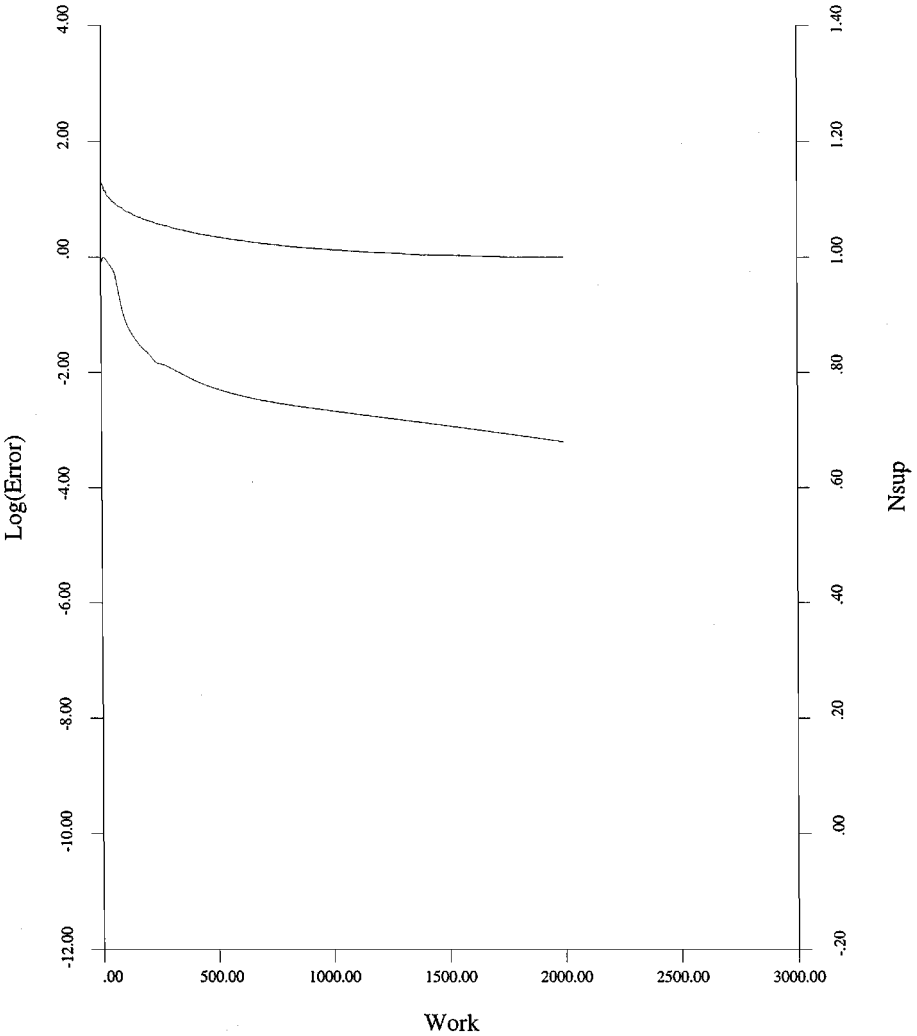

FIG. 17. Single grid convergence history: $M = 2.10$ hydrogen/air 6.34° viscous ramp. Grid size, 128×96.

OH is being consumed and transformed to water. This is due to the higher temperature in the boundary layer near the wall, and because the molecules in that region have a longer residence time at those higher temperatures due to the lower velocity near the wall. The maximum water mass fraction is approximately 3%, which is not much greater than the free stream water mass fraction from Table 1. This small amount of water production and heat release is not sufficient to cause thermal runaway, greater reaction, and greater heat release. These results agree qualitatively with the experimental findings. Excited OH fluorescence was observed in the region behind the shock and near the leading edge, but large regions of heat release were absent.

Figures 17 and 18 show convergence histories for this calculation without and with multigrid acceleration. The single grid calculation converged approximately three orders of magnitude in 2000 iterations. The computational cost of this calculation was 4578 seconds using six processors of an IBM SP. The multigrid calculation with two levels of grids converged six orders of magnitude after 2000 iterations in 7992 seconds of wall clock time.

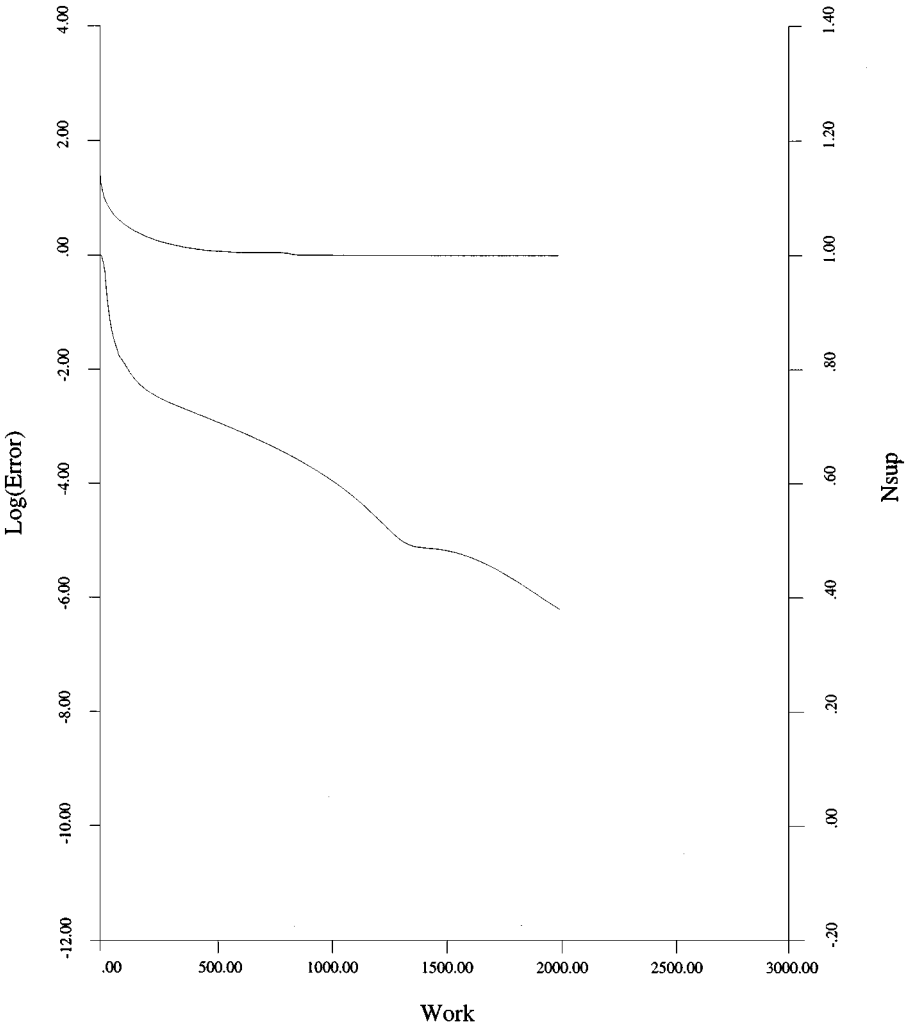

FIG. 18. Multigrid convergence history: $M = 2.10$ hydrogen/air 6.34° viscous ramp. Grid size, 128×96.

The multigrid calculation achieved the same convergence level as the single grid calculation in approximately 2550 seconds, which is 1.80 times faster than the single grid calculation. The results of both simulations are virtually identical. As in the inviscid case presented previously, no unphysical diffusion of species is seen due to the correct forcing of the coarse grid.

The third test case consisted of a stoichiometric hydrogen/air flow over a 10° viscous ramp. The freestream Mach number was 4.0, the freestream temperature was 1200 K, and the freestream pressure was one atmosphere. The 2-cm ramp was preceded by a 1-cm solid wall section. The effects of viscosity, heat conduction, and species diffusion are all included in this computation. This is a common viscous/reactive test case, with several published computations available [4, 18, 32, 40] for turbulent reactive flows. However, because of the lack of concrete knowledge regarding the effect of turbulence on combustion, in this work the flow was computed assuming fully laminar flow. This will produce different results than those obtained using a turbulence model, but a grid convergence study may

still be pursued to determine the robustness of the numerical model. In addition, most of the researchers who attempted this computation used grids leading to solutions that were severely underresolved, both in the boundary layer region and in the reaction zone. Thus, any results that were obtained must be viewed in this light.

This flow was computed using Westbrook's nine species, seventeen reaction hydrogen/air mechanism because other researchers have used this model for this test case. This is a very challenging flow because of the myriad of physical phenomena that must be resolved accurately. The formation of the boundary layer must be captured well, without unnecessary dissipation, so that the displacement thickness is correct. The conduction of heat must also be accurate so that the effects of viscous dissipation deep in the boundary layer are felt correctly in the sections of the boundary layer far from the wall. Proper resolution of the interaction of the shock and boundary layer and the oscillation free capture of the shock are essential, as is the correct modeling of species diffusion. The free stream temperature is not high enough to initiate a reaction, but the combination of high temperature in the boundary layer, diffusion of radicals in the direction normal to the wall, and the oblique shock cause a reaction front to form past the shock in the ramp region.

An assiduous grid convergence study was undertaken for this flow. Three grids were used to simulate this flow and to determine the robustness of the algorithm. All three grids had cells clustered near the wall to properly capture the laminar boundary layer, with approximately 32 cells within the boundary layer. In addition, cells were clustered near the start of the ramp, where shock-boundary layer interaction may lead to interesting phenomena. We would expect any artificial diffusion of mass, momentum, and energy to decrease as the grid resolution increases. In addition, the modeling of convective and diffusive transport is second order accurate and thus, the accuracy of the physical transport should increase as the grid spacing becomes smaller. Figures 19, 20, and 21 show the temperature in the flow field for three grids of size 64×96, 64×108, and 128×156, with the first number of cells along the wall and the second number of cells normal to the wall. As was expected, the formation of the boundary layer and the attendant viscous dissipation raises the temperature near the wall which causes various radical species to form. This leads to the formation of some water

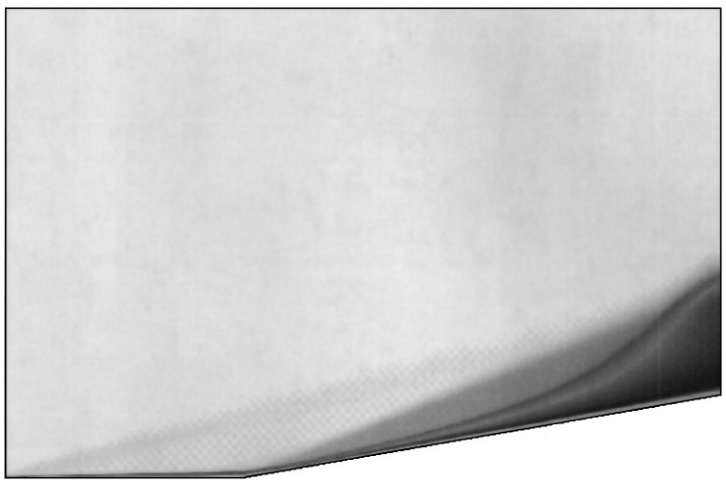

FIG. 19. Temperature: $M = 4.0$ hydrogen/air 10° viscous ramp, 64×96 grid. Temperature range, 1200–3500 K.

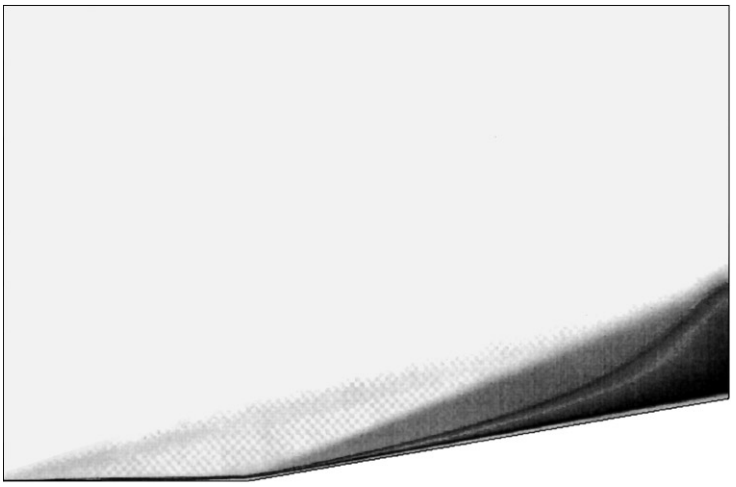

FIG. 20. Temperature: $M = 4.0$ hydrogen/air 10° viscous ramp, 64×108 grid. Temperature range, 1200–3500 K.

vapor very near the wall before the shock, but does not greatly affect the flowfield. One may also notice the formation of a weak oblique shock at the left edge of the domain due to the displacement thickness of the boundary layer. The interaction of the stronger oblique shock and the boundary layer at the ramp corner separates the boundary layer for a short distance and causes a small recirculation zone in that region. Beyond the oblique shock, the increased temperature and pressure lead to faster radical production and increased diffusion of those radicals and heat to the unreacted bulk flow behind the shock. The result is a reaction front that forms and gradually moves away from the wall. The reaction front may be seen in a different way by viewing the mass fraction of water in Fig. 22 for the 128×156 grid. Comparing the results of the three grid simulations yields interesting insights into the resolution needed for this flow. The third grid (128×156) has twice the resolution of the first grid

FIG. 21. Temperature: $M = 4.0$ hydrogen/air 10° viscous ramp, 128×156 grid. Temperature range, 1200–3500 K.

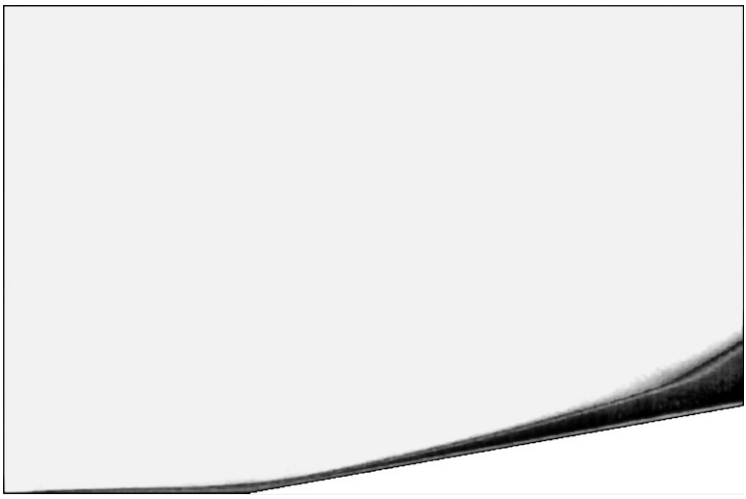

FIG. 22. Water mass fraction: $M = 4.0$ hydrogen/air 10° viscous ramp, 128×156 grid. Mass fraction range, 0.00–0.18.

(64×96) in both the normal and streamwise directions outside of the boundary layer. The result is that the reaction front is unphysically diffused on the coarser grid (due to inadequate resolution of the reaction zone, artificial diffusion of radical species and energy, and inadequate resolution for diffusive transport) and is captured quite well on the finest grid. The curvature of the reaction front at the right edge of the domain may be an actual physical phenomenon or it may be a numerical artifact. If it is a spurious numerical phenomenon, it is probably due to one of two causes. First, it may be that the supersonic extrapolation boundary conditions at the outflow plane are contaminating the solution. Second, the numerical dissipation may be causing unphysical diffusion of radical species and heat. However, it is unlikely, given the resolution of this grid in that particular area, that the artificial dissipation is the cause. Thus, in order to test the accuracy of the boundary condition, an additional simulation was performed in which the outflow plane of the simulation domain was moved approximately 0.9 cm downstream. The computational size of this additional simulation was also 128×156 cells, with 32 cells again within the boundary layer.

The results of this extended domain simulation are presented in Figs. 23–25. The flow field temperature is depicted in Fig. 23, where the solid line within the simulation domain indicates the former outflow plane location. Comparing this figure to Fig. 21, one can see that the temperature in the smaller domain and the extended domain match exceptionally well in the original computational region. Water mass fraction is shown in Fig. 24, while pressure may be viewed in Fig. 25. The extension of the domain makes it evidently clear that the curvature of the reaction front observed in Figs. 21 and 22 is indeed a true physical phenomenon. In addition, the simulation on the extended domain indicates that the use of supersonic extrapolation boundary conditions at the outflow plane does not compromise the accuracy of the solution in the region of the boundary. In this flow, radicals and heat in the boundary layer diffuse outward normal to the wall and eventually, along with the increased temperature and pressure behind the oblique shock, cause the reaction to proceed in the inviscid region behind the oblique shock. This reaction front couples with the shock toward the outflow plane and changes the angle of the discontinuity in the flow due to the pressure and heat release behind the shock/reaction front.

FIG. 23. Temperature for extended domain: $M = 4.0$ hydrogen/air 10° viscous ramp, 128×156 grid. Temperature range, 1200–3500 K. Solid line in the computational domain indicates original outflow boundary.

FIG. 24. Water mass fraction for extended domain: $M = 4.0$ hydrogen/air 10° viscous ramp, 128×156 grid. Mass fraction range, 0.00–0.18.

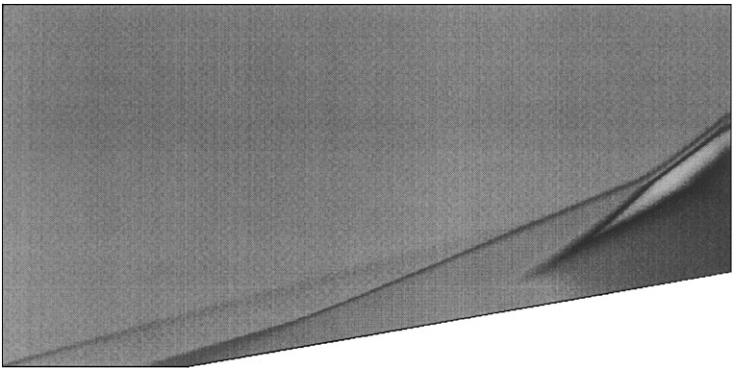

FIG. 25. Normalized pressure for extended domain: $M = 4.0$ hydrogen/air 10° viscous ramp, 128×156 grid. Normalized pressure range, 0.00–6.00.

Other researchers' previously published results [4, 18, 32, 40] for this flow were calculated on coarser grids than the finest grid presented here. These previous simulations show a coupled shock reaction front located much closer to the ramp corner in which the shock curves away from the wall. While these other simulations were computed with turbulence models of varying complexity, it is probably the underresolution of the reaction area which leads to the greatest disparity between those results and those presented here. If the reaction area is underresolved and the numerical scheme is too dissipative, then a probable result would be for the reaction zone to move upstream to the shock position. This would be caused by unphysical diffusion of radical species and thermal energy upstream, allowing the reaction to commence earlier and thus move toward the shock. In fact, early simulations of this flow field with the current method using a very coarse grid were characterized by the reaction front moving upstream and away from the wall toward the shock location.

7. CONCLUSIONS

An accurate solver for the steady-state Euler and Navier–Stokes equations with chemical reactions has been developed. It is found that the CUSP dissipation scheme yields accurate capture of shocks, reaction zones, and reaction fronts for both inviscid axisymmetric and viscous two-dimensional test cases while the use of multigrid acceleration techniques leads to a significant decrease in computational time without sacrificing accuracy. The combination of the accuracy and parallel efficiency of the method allows the simulation of large scale problems that would otherwise not be feasible.

APPENDIX: NOMENCLATURE

$\mathbf{C}(\mathbf{w}_{ij})$	convective Euler fluxes for cell i, j
$c_{i+\frac{1}{2}}$	speed of sound at interface $i+\frac{1}{2}$
$\mathbf{D}(\mathbf{w}_{ij})$	dissipative fluxes for cell i, j
D_i	diffusion coefficient for species i
D_{ij}	binary diffusion coefficient between species i and j
$\mathbf{d}_{i+\frac{1}{2}}$	artificial diffusive flux at cell interface $i+\frac{1}{2}$
$\mathbf{d}'_{i+\frac{1}{2}}$	modified artificial diffusive flux at cell interface $i+\frac{1}{2}$
$\mathbf{d}_{c_{i+\frac{1}{2}}}$	artificial dissipation convective flux at cell interface $i+\frac{1}{2}$
$\mathbf{d}_{p_{i+\frac{1}{2}}}$	artificial dissipation pressure flux at cell interface $i+\frac{1}{2}$
E	mass specific total energy (internal, chemical, and kinetic)
E_{Aj}	activation energy for jth forward reaction
e	mass specific mixture internal and chemical energy
$\mathbf{f}, \mathbf{g}$	Euler flux vectors
$\mathbf{f}_c, \mathbf{f}_p$	convective and pressure split vectors
$\mathbf{f}_\mathbf{v}, \mathbf{g}_\mathbf{v}$	diffusive flux vectors
$\mathbf{G}_k$	multigrid forcing function
H	mixture total enthalpy
h_i	mass specific static enthalpy of species i
$I'_{k-1,k}$	multigrid limited interpolation operator
K_{c_j}	equilibrium constant for concentration for reaction j
K_{p_j}	equilibrium constant for partial pressures for reaction j

k_{f_j}, k_{r_j}	forward and reverse rate coefficients for reaction j
L	a limiter
M	Mach number
$\mathbf{NS}(\mathbf{w}_{ij})$	diffusive fluxes for cell i, j
$P_{k,k-1}$	multigrid transfer operator from grid level $k-1$ to level k
p	static pressure
$Q_{k,k-1}$	multigrid residual collection transfer operator
$\mathbf{q}$	conductive heat flux vector
R	mixture gas constant
$\mathcal{R}$	universal gas constant
$\mathbf{R}(\mathbf{w}_{ij})$	total flux residual for cell i, j
$\mathbf{R}'(\mathbf{w}_{ij})$	modified flux residual for cell i, j
T	static temperature
u, v	Cartesian velocity components
$\mathbf{u}_{di}$	diffusion velocity vector for species i
u_{di}, v_{di}	diffusion velocity components for species i
V_{ij}	volume of cell i, j
$\mathbf{w}$	vector of conservative flow variables
$\Delta\mathbf{w}_{i+\frac{1}{2}}$	central difference of flow variables at cell interface
X_i	mole fraction of species i
α_k	weighting for stage k of multistage time stepping scheme
γ	mixture ratio of specific heats
θ_u	multigrid underrelaxation factor
ρ	density
ρ_i	density of species i
τ	viscous stress
$\dot{\omega}$	chemical source term
$\Omega, \partial\Omega$	cell element and boundary
∇	gradient operator

ACKNOWLEDGMENTS

This work was funded by AFOSR-URI F49620-93-1-0427. The first author was supported in part by a Fannie and John Hertz Foundation/Princeton Research Center Fellowship.

REFERENCES

1. A. A. Belov, *A New Implicit Multigrid-Driven Algorithm for Unsteady Incompressible Flow Calculations on Parallel Computers*, Ph.D. thesis, Department of Mechanical and Aerospace Engineering, Princeton University, June 1997.
2. T. R. A. Bussing and E. M. Murman, Numerical investigation of two-dimensional H_2-air flameholding over ramps and rearward-facing steps, *J. Propulsion* **3**(5), 448 (1987).
3. T. R. A. Bussing and E. M. Murman, Finite-volume method for the calculation of compressible chemically reacting flows, *AIAA J.* **26**(9), 1070 (1988).
4. T. Chitsomboon, A. Kumar, and S. N. Tiwari, *Numerical Study of Finite-Rate Supersonic Combustion Using Parabolized Equations*, AIAA paper 87-0088, AIAA 25th Aerospace Sciences Meeting and Exhibit, Reno, NV, January 1987.

5. J. D. Denton, An improved time marching method for turbomachinery flow calculations, *J. Eng. Gas Turbines Power* **105** (1983).
6. S. Eberhardt and S. Imlay, Diagonal implicit scheme for computing flows with finite rate chemistry, *J. Thermophysics Heat Transfer* **6**, 208 (1992).
7. D. R. Eklund, J. P. Drummond, and H. A. Hassan, Efficient calculation of chemically reacting flow, *AIAA J.* **25**(6), 855 (1987).
8. D. R. Eklund, J. P. Drummond, and H. A. Hassan, Calculation of supersonic turbulent reacting coaxial jets, *AIAA J.* **28**(9), 1633 (1990).
9. J. S. Evans and C. J. Schexnayder, Influence of chemical kinetics and unmixedness on burning in supersonic hydrogen flames, *AIAA J.* **18**(2), 180 (1980).
10. J. Fielding, *An Experimental Study of Supersonic Laminar Reacting Boundary Layers*, Master's thesis, Department of Mechanical and Aerospace Engineering, Princeton University, January 1997.
11. W. C. Gardiner, Jr. (Ed.), *Combustion Chemistry* (Springer-Verlag, New York, 1984).
12. C. W. Gear, *Numerical Initial Value Problems in Ordinary Differential Equations* (Prentice Hall, New York, 1971).
13. C. J. Jachimowski, *An Analytical Study of the Hydrogen-Air Reactions Mechanism with Application to Scramjet Combustion*, NASA TP 2791, 1988.
14. A. Jameson, Solution of the Euler equations for two dimensional transonic flow by a multigrid method, *Appl. Math. Comp.* **13**, 327 (1983).
15. A. Jameson, Multigrid algorithms for compressible flow calculations, in *Proceedings of the 2nd European Conference on Multigrid Methods, Cologne, 1985*, edited by W. Hackbusch and U. Trottenberg, Lecture Notes in Math. (Springer-Verlag, New York/Berlin, 1986), Vol. 1228, p. 166.
16. A. Jameson, Analysis and design of numerical schemes for gas dynamics. 1. Artificial diffusion, upwind biasing, limiters and their effect on multigrid convergence, *Int. J. Comp. Fluid Dyn.* **4**, 171 (1995).
17. A. Jameson, Analysis and design of numerical schemes for gas dynamics. 2. Artificial diffusion and discrete shock structure, *Int. J. Comp. Fluid Dyn.* **5**, 1 (1995).
18. Y. Ju, Lower-upper scheme for chemically reacting flow with finite rate chemistry, *AIAA J.* **33**(8), 1418 (1995).
19. R. J. Kee, G. Dixon-Lewis, J. Warnatz, M. E. Coltrin, and J. A. Miller, *A Fortran Computer Code Package for the Evaluation of Gas-Phase Multicomponent Transport Properties*, SAND 86-8246, Sandia National Laboratories, Livermore, CA, May 1993.
20. T. J. Kim, R. A. Yetter, and F. L. Dryer, New results on moist CO oxidation: High pressure, high temperature experiments and comprehensive kinetic modeling, in *Twenty-Fifth Symposium (International) on Combustion, The Combustion Institute, 1994.*
21. H. F. Lehr, Experiments on shock-induced combustion, *Astronautica Acta* **17**, 589 (1972).
22. M.-S. Liou and C. J. Steffen, Jr., A new flux splitting scheme, *J. Comput. Phys.* **107**, 23 (1993).
23. L. Martinelli, *Calculation of Viscous Flows with a Multigrid Method*, Ph.D. thesis, Department of Mechanical and Aerospace Engineering, Princeton University, October 1987.
24. L. Martinelli and A. Jameson, *Validation of a Multigrid Method for the Reynolds Averaged Equations*, AIAA paper 88-0414, AIAA 26th Aerospace Sciences Meeting, Reno, NV, January 1988.
25. A. Matsuo and T. Fujiwara, Numerical investigation of oscillatory instability in shock-induced combustion around a blunt body, *AIAA J.* **31**(10), 1835 (1993).
26. A. Matuso, K. Fujii, and T. Fujiwara, Flow features of shock-induced combustion around projectile traveling at hypervelocities, *AIAA J.* **33**(6), 1056 (1995).
27. E. S. Oran and J. P. Boris, *Numerical Simulation of Reactive Flow* (Elsevier, Amsterdam, 1987).
28. G. Palmer and E. Venkatapathy, Comparison of nonequilibrium solution algorithms applied to chemically stiff hypersonic flows, *AIAA J.* **33**(7), 1211 (1995).
29. S. G. Sheffer, *Parallel Computation of Supersonic Reactive Flows with Detailed Chemistry Including Viscous and Species Diffusion Effects*, Ph.D. thesis, Department of Mechanical and Aerospace Engineering, Princeton University, June 1997.

30. S. G. Sheffer, A. Jameson, and L. Martinelli, *A Multigrid Method for High Speed Reactive Flows*, AIAA paper 97-2106, AIAA 13th Computational Fluid Dynamics Conference, Snowmass Village, CO, June 29–July 2, 1997.
31. S. G. Sheffer, A. Jameson, and L. Martinelli, *Parallel Computation of Supersonic Reactive Flows with Detailed Chemistry*, AIAA paper 97-0899, AIAA 35th Aerospace Sciences Meeting, Reno, NV, January 6–9, 1997.
32. J. S. Shuen and S. Yoon, Numerical study of chemically reacting flows using a lower-upper symmetric successive overrelaxation scheme, *AIAA J.* **27**(12), 1752 (1989).
33. M. A. Sussman, *Source Term Evaluation for Combustion Modeling*, AIAA paper 93-0239, AIAA 31st Aerospace Sciences Meeting and Exhibit, Reno, NV, January 11–14, 1993.
34. S. Tatsumi, L. Martinelli, and A. Jameson, *Design, Implementation, and Validation of Flux Limited Schemes for the Solution of the Compressible Navier–Stokes Equations*, AIAA paper 94-0647, AIAA 32nd Aerospace Sciences Meeting, Reno, NV, January 1994.
35. S. Tatsumi, L. Martinelli, and A. Jameson, *A New High Resolution Scheme for Compressible Viscous Flow with Shocks*, AIAA paper 95-0466, AIAA 33rd Aerospace Sciences Meeting and Exhibit, Reno, NV, January 9–12, 1995.
36. C. K. Westbrook, Hydrogen oxidation kinetics in gaseous detonations, *Combustion Sci. Tech.* **29**, 67 (1982).
37. F. A. Williams, *Combustion Theory* (Addison–Wesley, Reading, MA, 1985), 2nd ed.
38. G. J. Wilson and R. W. MacCormack, Modeling supersonic combustion using a fully implicit numerical method, *AIAA J.* **30**(4), 1008 (1992).
39. G. J. Wilson and M. A. Sussman, Computation of unsteady shock-induced combustion using logarithmic species conservation equations, *AIAA J.* **31**(2), 294 (1993).
40. H. C. Yee and J. L. Shinn, Semi-implicit and fully implicit shock-capturing methods for nonequilibrium flows, *AIAA J.* **27**(3), 299 (1989).
41. R. Yetter and J. Fielding, private communication, Princeton University, 1996.
42. R. A. Yetter, F. L. Dryer, and D. M. Golden, Pressure effects on the kinetics of high speed chemically reacting flows, in *Major Research Topics in Combustion*, ICASE/NASA Series (Springer-Verlag, New York, 1992).
43. S. Yungster, Numerical study of shock-wave/boundary-layer interactions in premixed combustible gases, *AIAA J.* **30**(10), 2379 (1992).
44. S. Yungster and A. P. Bruckner, Computational studies of a superdetonative ram accelerator mode, *J. Propulsion Power* **8**(2), 457 (1992).
45. S. Yungster, S. Eberhardt, and A. P. Bruckner, Numerical simulation of hypervelocity projectiles in detonable gases, *AIAA J.* **29**(2), 187 (1991).
46. S. Yungster and M. J. Rabinowitz, Computation of shock-induced combustion using a detailed methane-air mechanism, *J. Propulsion Power* **10**(5), 609 (1994).